

NAT'L INST. OF STAND & TECH



A11106 977750

NIST
PUBLICATIONS

REFERENCE

NISTIR 6645

Thermodynamic Properties of 1-hexyl- 3-methylimidazolium bis(trifluoromethylsulfonyl)imide

D.G. Archer

QC
100
.456
#6645
2006

NIST

National Institute of Standards and Technology
Technology Administration, U.S. Department of Commerce

NISTIR 6645

Thermodynamic Properties of 1-hexyl- 3-methylimidazolium bis(trifluoromethylsulfonyl)imide

D.G. Archer

*Physical and Chemical Properties Division
Chemical Science and Technology Laboratory*

November 2006



U.S. Department of Commerce
Carlos M. Gutierrez, Secretary

Technology Administration
Robert Cresanti, Under Secretary of Commerce for Technology

National Institute of Standards and Technology
William Jeffrey, Director

Contents

1. Introduction	1
2. Materials	2
3. Calibration of the Differential Scanning Calorimeter	2
4. Ionic Liquid Results	11
5. References	15

Thermodynamic Properties of 1-hexyl-3-methylimidazolium bis(trifluoromethylsulfonyl)imide

D. G. Archer

National Institute of Standards and Technology
Gaithersburg, Maryland 20899

Measurements of the heat capacity and the enthalpy changes of transitions of 1-hexyl-3-methylimidazolium bis(trifluoromethylsulfonyl)imide were requested as part of a project initiated by the International Union of Pure and Applied Chemistry (IUPAC). The measurements were performed with differential scanning calorimetry from 150 K to 345 K. These measurements led to the heat capacity of the crystal phases; the enthalpy change for transition between two crystal phases; the heat capacity of a glass, the supercooled liquid, and the stable liquid; the fusion temperatures of two crystal phases; and the enthalpy change for fusion of the stable crystal phase. Measurements at higher temperatures also probed thermal stability of the material. The calibration of the differential scanning calorimeter is described in detail.

Keywords: crystal, enthalpy, fusion, glass, heat capacity, 1-hexyl-3-methylimidazolium bis(trifluoromethylsulfonyl)imide, ionic liquid, liquid, thermodynamics

1. Introduction

Measurements of the thermodynamic properties of 1-hexyl-3-methylimidazolium bis(trifluoromethylsulfonyl)imide were requested by the IUPAC coordinator to be made with differential scanning calorimetry (DSC). These DSC measurements were made contemporaneously with measurements made in other laboratories that used adiabatic calorimetry and differential scanning calorimetry.

Differential scanning calorimetry has advantages and disadvantages relative to traditional adiabatic enthalpy-increment calorimetry. DSC requires significantly less sample than does adiabatic calorimetry. The smaller sample and addenda allow for examination of phenomena with faster kinetic effects than those observable with adiabatic calorimetry. The small sample and addenda size in DSC also can allow for much faster changes in temperature, both in heating and cooling, thereby allowing for greater latitude in studying the effects of temperature quenching. Additionally, DSC can yield quantitative information during controlled cooling. On the other hand, commercial differential scanning calorimeters do not have sufficient cooling capacity to temper materials for as extended a time as is possible with adiabatic calorimeters.

2. Materials

Ionic liquid. The ionic liquid, 1-hexyl-3-methylimidazolium bis(trifluoromethylsulfonyl)imide, was delivered sealed in a glass tube with a teflon valve. The ionic liquid sample was reported as having a purity of 99.5 % on the basis of hydrogen and fluorine nuclear magnetic resonance measurements. Water content was reported as being less than 20 ppm by coulometric Karl Fischer titration. The sample was used with no further purification. The original tube containing the ionic liquid was placed in an environmental chamber that had a drying train that utilized molecular sieves. The environmental chamber was first swept with nitrogen in order to remove the bulk of the oxygen from the chamber. However, the atmosphere processing train was not capable of reducing oxygen to still lower levels. For measurements, samples of the liquid were sealed hermetically in aluminum pans obtained from the manufacturer of the scanning calorimeter. The quantity of ionic liquid sealed in the various sample pans varied approximately from 2 mg to 15 mg.

Calibration materials. Cyclohexane was Spectro A.C.S. grade from Eastman Kodak.* Mercury was taken from a sample of SRM 2225. Water was de-ionized and reverse-osmosis treated in a central utility and then treated in the laboratory with a process that removed organics and conducted additional deionization. Indium was taken from two different samples; one was the material used for SRM 2232, the other was from a piece of shot from the lot of material whose properties were measured by Archer and Rudtsch [1]. Tin was also taken from two different samples; one was from a sample of SRM 2220, and the other was from a sample obtained from the Physikalisch-Technische Bundesanstalt (PTB). Zinc was obtained from a sample of SRM 2221a. Synthetic sapphire was taken from a sample of SRM 720 and was calcined prior to use.

3. Calibration of the Differential Scanning Calorimeter

Differential scanning calorimetry requires calibration of both the heat-flux scale and the temperature scale of the instrument. At some level, the accuracy achievable using DSC is a direct consequence of the limitations of calibration protocols and available reference materials. We used for the present work a multipoint calibration of both the temperature and heat-flux scales of the calorimeter. Differential scanning calorimeters that have been available commercially for at least the last 10 to 15 years have calibration software modules that hold calibration and other information. In the present work, we have not incorporated our calibration data into those modules, preferring not to limit ourselves to any particular calibration regimen. Indeed, there are parameters stored in our instrument's calibration routines, and we have not bothered to alter these because we intended to process much of our data outside of the data analysis routines that are in the instrument's controller package.

The temperature reported by a differential scanning calorimeter is susceptible to error inherent in the temperature measurement itself and also to an error that results from the kinetic lag between the temperature of the specimen and that of the thermometer because the specimen and

* Certain commercial materials and suppliers are identified in this paper in order to adequately specify the experimental procedure. Such identification does not imply recommendation or endorsement by either the U.S. Government or the National Institute of Standards and Technology, nor does it imply that the equipment or materials identified are necessarily the best available for the purpose.

Table 1. Literature values for the enthalpy change and temperature of the first-order crystal reorientation of cyclohexane.

$T_{\text{trs}} / \text{K}$	$\Delta_{\text{trs}}H / (\text{J}\cdot\text{g}^{-1})$	Reference
186.10	80.08	[2]
186.09	79.46	[3]
185.9	79.78	[4]

thermometer are not co-located. The temperature calibration was performed first by measuring the onset temperatures for several first-order phase transitions determined at scan rates, β , ranging from $1 \text{ K}\cdot\text{min}^{-1}$ to $10 \text{ K}\cdot\text{min}^{-1}$. The onset temperatures for each of the first-order phase transitions were extrapolated to a zero scan rate by means of first-order polynomials in order to determine the scan-rate-independent portion of the temperature error. The first-order transitions used for calibration were the crystal reorientation of cyclohexane and the fusion temperatures of mercury, ice, indium, tin, and zinc. Literature values for the crystal transition of cyclohexane are given in Table 1; from these we took 186.10 K as the fusion temperature for cyclohexane. We used established ITS-90 temperatures for the fusions of ice, indium, and zinc. For mercury, we used $T_{\text{fus}} = (234.32 \pm 0.03) \text{ K}$, which is the ITS-90 value combined with the uncertainty attached to the SRM 2225 certification. Combination of the certified temperature of fusion, presumably on the IPTS-68, with an adjustment from the ITS-90, gave $T_{\text{fus}} = 234.31 \text{ K}$. Within the uncertainty assigned, these two values are indistinguishable.

The scan-rate independent portion of the temperature error is shown in Figure 1(a), where the error bars shown are one standard deviation for the $\beta = 0$ intercepts obtained from the first-order polynomial representations. Also shown is the function used to represent the scan-rate-independent portion, εT_0 , of the total temperature error, εT , for correction of the temperatures of subsequent measurements. The function used for the representation had the form

$$\varepsilon T_0/T^\circ = a + b(T/T^\circ) + c(T/T^\circ)^{-2} , \quad (1)$$

where T° is 1 K.

The values leading to εT_0 are given in Table 2 and the individual measurements and fitted parameters are given in Table 3. The scan-rate dependent portion of the temperature error, taken from the slopes of the first-order polynomial representations of the onset temperatures for the first-order phase transitions, is shown in Figure 1(b). The error bars are the 95 % confidence intervals from the least-squares representations. A statistically significant dependence of these values on temperature was not observed and we therefore used the negative of the mean value (-0.094 min) for correction of the scan-rate-dependent portion of the temperature error.

Table 2. Temperature calibration data.

Substance	$T(\text{onset}) / \text{K}$	$T(\text{literature}) / \text{K}$	Difference / K
Cyclohexane	188.0 ± 0.20	186.1	-1.9
Mercury	234.90 ± 0.29	234.30 ± 0.03	-0.60
Water	273.43 ± 0.43	273.15	-0.28
Indium	429.76 ± 0.08	429.749	-0.01
Indium	429.82 ± 0.10	429.749	-0.04
Tin	505.48 ± 0.11	505.07 ± 0.01	-0.41
Tin	505.43 ± 0.047	505.07 ± 0.01	-0.36
Zinc	693.78 ± 0.20	692.677	-1.10

Table 3. Calibration data from first-order transitions.

$\beta / (\text{K} \cdot \text{min}^{-1})$	$T(\text{onset}) / \text{K}$	$\Delta_{\text{fus}}h / (\text{J} \cdot \text{g}^{-1})$
	Tin (sample 1)	
10	506.43	63.43
10	506.43	63.38
10	506.46	63.47
10	506.42	63.50
10	506.28	63.47
10	506.36	63.44
10	506.27	63.50
10	506.28	63.53
5	505.91	63.54
5	505.90	63.53
5	505.91	63.54
2	505.68	63.56
2	505.67	63.58
2	505.67	63.59
1	505.55	63.54
1	505.55	63.59
Average $\Delta_{\text{fus}}h$		63.51 ± 0.03
intercept	$(505.48 \pm 0.11) \text{ K}$	
slope	$(0.089 \pm 0.0020) \text{ K} \cdot \text{min}^{-1}$	

Table 3. Calibration data from first-order transitions (cont.).

$\beta / (\text{K}\cdot\text{min}^{-1})$	$T(\text{onset}) / \text{K}$	$\Delta_{\text{fus}}h / (\text{J}\cdot\text{g}^{-1})$
	Tin (sample 2)	
10	506.26	
10	506.27	
5	505.81	
5	505.81	
3	505.71	
3	505.68	
3	505.62	
1	505.55	
1	505.51	
1	505.51	
1	505.53	
Intercept	(505.43 \pm 0.047) K	
slope	(0.082 \pm 0.002) K \cdot min $^{-1}$	
	Indium (sample 1)	
10	430.93 ^a	30.61
10	430.59	30.65
10	430.51	30.66
5	430.15	30.74
5	430.21	30.78
3	430.01	30.69
3	430.14	30.69
1	429.86	30.75
1	429.90	30.73
1	429.89	30.78
10	430.63	30.66
Average $\Delta_{\text{fus}}h$		30.70 \pm 0.03
intercept	(429.82 \pm 0.10) K	
slope	(0.076 \pm 0.003) K \cdot min $^{-1}$	

Table 3. Calibration data from first-order transitions (cont.).

$\beta / (\text{K min}^{-1})$	$T(\text{onset}) / \text{K}$	$\Delta_{\text{fus}}h / (\text{J}\cdot\text{g}^{-1})$
Indium (sample 2)		
10	430.80	
10	430.84	
10	430.75	
10	430.86	
5	430.30	
5	430.31	
1	429.84	
1	429.85	
3	430.09	
3	430.09	
Intercept	$(429.76 \pm 0.08) \text{ K}$	
slope	$(0.106 \pm 0.002) \text{ K}\cdot\text{min}^{-1}$	
Mercury		
1	235.52 ^a	12.59
1	234.97	12.59
1	234.91	12.60
3	235.30	12.59
3	235.16	12.60
3	235.15	12.60
5	235.47	12.57
1	234.95	12.64
10	236.18	12.73
5	235.51	12.53
10	236.28	12.68
Average $\Delta_{\text{fus}}h$	12.61 ± 0.03	
intercept	$(234.78 \pm 0.095) \text{ K}$	
slope	$(0.143 \pm 0.003) \text{ K}\cdot\text{min}^{-1}$	

Table 3. Calibration data from first order transitions (cont.).

$\beta / (\text{K min}^{-1})$	$T(\text{onset}) / \text{K}$	$\Delta_{\text{fus}}h / (\text{J}\cdot\text{g}^{-1})$
Cyclohexane		
Crystal reorientation		
10	188.75	94.22
10	188.78	94.55
5	188.35	94.10
5	188.28	94.27
2	188.18	94.16
2	188.21	94.08
Average $\Delta_{\text{fus}}h$		94.23 ± 0.14
intercept	$(188.01 \pm 0.22) \text{ K}$	
slope	$(0.073 \pm 0.005) \text{ K}\cdot\text{min}^{-1}$	
Zinc		
10	694.69	111.8
10	694.52	111.9
5	694.16	112.0
5	694.09	112.0
3	693.88	112.2
3	694.00	112.1
1	693.94	111.8
1	693.94	111.8
10	694.55	111.5
Average $\Delta_{\text{fus}}h$		111.9 ± 0.14
intercept	$(693.78 \pm 0.203) \text{ K}$	
slope	$(0.078 \pm 0.005) \text{ K}\cdot\text{min}^{-1}$	
Water		
10	274.67	
10	274.43	
5	274.08	
3	273.69	
3	273.67	
1	273.71	
Intercept	$(273.47 \pm 0.43) \text{ K}$	
slope	$(0.107 \pm 0.011) \text{ K}\cdot\text{min}^{-1}$	

All \pm values are 95% confidence intervals.

^a signifies a point not included in the data representation.

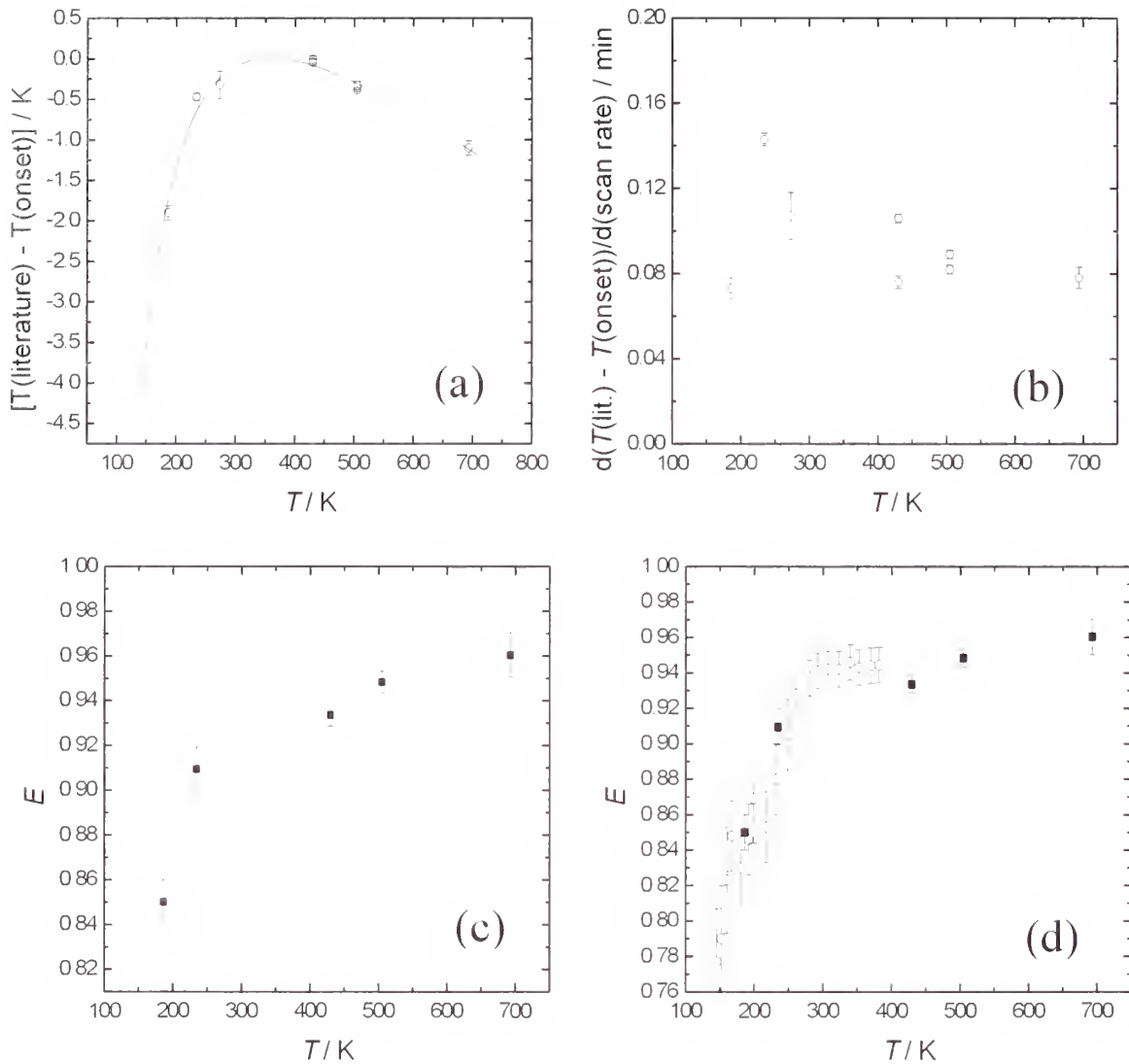


Figure 1. Calibration information for the calorimetric measurements. (a) Difference of the onset temperatures, extrapolated to zero scan rate, $\beta = 0$, from the reference values. Also shown is the representation of these values for use in correction of temperatures reported by the calorimeter. (b) Dependence of the onset temperature on scan rate. (c) Values of the heat-flux calibration constant, E , calculated from the first-order phase transitions. (d) Values of the heat-flux calibration constant calculated from measurements on SRM 720, after proper correction for the temperature-scale error, and values from the first-order phase transitions. The values from the first-order phase transitions are shown by solid symbols. Empty symbols show representative average values from the heat capacity measurements for SRM 720.

In order to calibrate the heat-flux scale of the calorimeter, we measured enthalpy changes accompanying the first-order crystal-crystal phase transition of cyclohexane and the fusions of mercury, indium, tin, and zinc. The reference value used for cyclohexane was the value from Ruehrwein and Huffman [2]. We note that their value is approximately 0.8 % different from the value from Aston et al. [3] and approximately 0.4 % different than the earlier value reported by Parks and Huffman [4]. We didn't consider the values from Ziegler and Andrews [5] to be equally reliable. Clearly, the uncertainty arising from the choice of a reference value for this transition is much larger than the standard deviation of the means, 0.07 %, obtained from the calibration measurements using cyclohexane. The reference value used for mercury, SRM 2225, was the Certificate value, $(11.469 \pm 0.008) \text{ J}\cdot\text{g}^{-1}$. For indium, we used the value determined by Archer and Rudtsch [1], $\Delta_{\text{fus}}h = (28.6624 \pm 0.0076) \text{ J}\cdot\text{g}^{-1}$. For tin, SRM 2220, the Certificate value was used, $\Delta_{\text{fus}}h = (60.22 \pm 0.12) \text{ J}\cdot\text{g}^{-1}$. For zinc, we used the value determined by Ditmars [6] for SRM 2221a, $\Delta_{\text{fus}}h = (107.46 \pm 0.12) \text{ J}\cdot\text{g}^{-1}$. The specific enthalpy changes observed with the calorimeter were calculated using sigmoidal baselines and are given in Table 3. No significant dependence of observed enthalpy of transition on the temperature scan rate was observed. A correction factor for the heat flux, E , was calculated as

$$E = \Delta h(\text{reference})/\Delta h(\text{observed}) \quad . \quad (2)$$

The values of E obtained from the first-order phase transitions are shown in Figure 1(c). The 95 % confidence intervals of the means were generally about 0.1 %, and are included in Table 3. The uncertainties shown as error bars in Figure 1(c) are from the 95 % confidence intervals of the populations combined with an estimated or stated uncertainty of the reference value. This method overestimates the uncertainty in so far as the proper calculation would include the statistic for the means rather than the statistic for the population. Only for the case of cyclohexane do we consider that the reference value contributes significantly to the uncertainty of the value of E .

The rapid decrease of E at low temperatures was observed previously for our instrument [7]. This low-temperature behavior was confirmed and further quantified with stepwise heating intervals for a sample of synthetic sapphire, SRM 720. All measurements of heat capacity for SRM 720 and for the ionic liquid were made with a nominal scan rate of $5 \text{ K}\cdot\text{min}^{-1}$. The heat capacity values for SRM 720 that were used as reference values were those given by Archer [8], as those values are consistent with the ITS-90. When comparing E values obtained from a heat capacity standard with E values obtained from first-order phase transitions, one must take into account the temperature-scale error for the instrument, as these will affect the former but not the latter. More specifically, the instrument records heat flux, \dot{Q} , in units of mW, or $\text{mJ}\cdot\text{s}^{-1}$. To obtain a specific heat capacity, c , without consideration of the error in the observed heat flux, one would divide the heat flux by the scan rate, β , converting to seconds, as

$$c = \dot{Q}/(\beta \cdot 60 \text{ s/min}) \quad . \quad (3)$$

The instrument controls the scan rate, β , by means of its temperature sensor and software. However, as shown in the temperature-scale calibration of the instrument, there is error in the temperature reported by the instrument, and hence there is error in the value of β . In other words, the true scan rate of the instrument is not necessarily that chosen and controlled, β , but is some quantity $(\beta + \delta\beta)$, where $\delta\beta$ is calculated from the temperature-scale calibration

information. This error is *not* necessarily small; at 150 K for this particular calorimeter in its current state of calibration, the value of heat capacity that would be obtained from Eq. (3) would be in error by approximately 7 %; an error much greater than the uncertainties of any of the values of E obtained from the first-order phase transitions. Therefore, if one were not to consider properly the effect of the temperature-scale error on the specific heat calculation, then that miscalculation could lead to discrepancies between calibration coefficients obtained from enthalpy of transition measurements on the one hand, and heat-flux measurements (e.g., heat capacity measurements), on the other. The true value of the scan rate is

$$\beta(\text{true}) = \beta(\text{instrument}) (1 + d\varepsilon T/dT) \quad , \quad (4)$$

where $\beta(\text{instrument})$ is the scan rate controlled and reported by the instrument and $(d\varepsilon T/dT)$ is the temperature derivative of the correction for the error in the temperature scale of the instrument. Therefore, in order to calculate E from the values produced by the instrument for the sample of SRM 720, one must perform the following calculations:

$$T = T(\text{observed}) + \varepsilon T \quad , \quad (5)$$

$$c = \dot{Q} / (\beta(\text{instrument}) (1 + d\varepsilon T/dT) \cdot 60 \text{ s/min}) \quad . \quad (6)$$

The quantity c in Eq. (6) is the heat capacity for the sample of sapphire plus a contribution from any mismatch in weights of the sample and reference sample-containers (which is normally kept small by proper selection of containers for the sample and reference). Values of E were calculated from the heat flux calibration measurements as

$$E = c_p(\text{reference})/c_p(\text{observed}) \quad , \quad (7)$$

where we have used heat capacity values for SRM 720 from Archer [8], as these are consistent with the ITS-90. Heat capacity values for aluminum, the sample pan material, were taken from ASTM International Standard Method E1269. The E values obtained for the sample of SRM 720 were an average of the data from six scans. Representative average values are shown in Figure 1(d) along with the E values from the phase-transition standards. At the lowest temperatures, the uncertainty in values of E obtained from the sapphire measurements increased somewhat due to difficulties in the liquid nitrogen control for the small step scans combined with the limited size of the isothermal periods. Regardless, there is a quantitative agreement of the calibration coefficients obtained from the heat-flux measurements with those obtained from the enthalpies of transition. The error bars shown for the values of E in Figure 1(d) obtained from the sapphire measurements are the spread of the individual six runs; they are not representative of a statistic such as the standard deviation of the means or a confidence interval.

4. Ionic Liquid Results

The thermal behavior of the ionic liquid manifests several different structural behaviors. A thermal curve obtained from heating a sample from 150 K to 323 K at $5 \text{ K}\cdot\text{min}^{-1}$ is shown in Figure 2 below. The glass undergoes the transition from glass to the supercooled liquid at approximately 189 K. Above 225 K, the sample undergoes an exothermic devitrification. Above 262 K, at least two and possibly three endothermic events are witnessed.

Part of the request from the IUPAC project coordinator was to provide heat capacity values for the liquid phase to high temperatures. It was specifically noted by them that literature values showed that ionic liquids of this class were stable to above 570 K [9]. Reports of stability temperatures above 550 K up to 700 K are not unusual for room-temperature ionic liquids. These decomposition temperatures are often determined in fast-scan thermogravimetric analysis (TGA) instruments, which measure the mass of the sample as temperature is rapidly ramped. The TGA values are taken often as the sole measure of thermal stability of the ionic liquids and are reported in the literature as establishing the “feasible temperature operating range for a particular fluid.” By these TGA temperatures, room temperature ionic liquids are claimed to be applicable for industrial use as high temperature solvents. However, conventional TGA detects only the mass change of the sample, and thereby the method detects only the loss of volatile

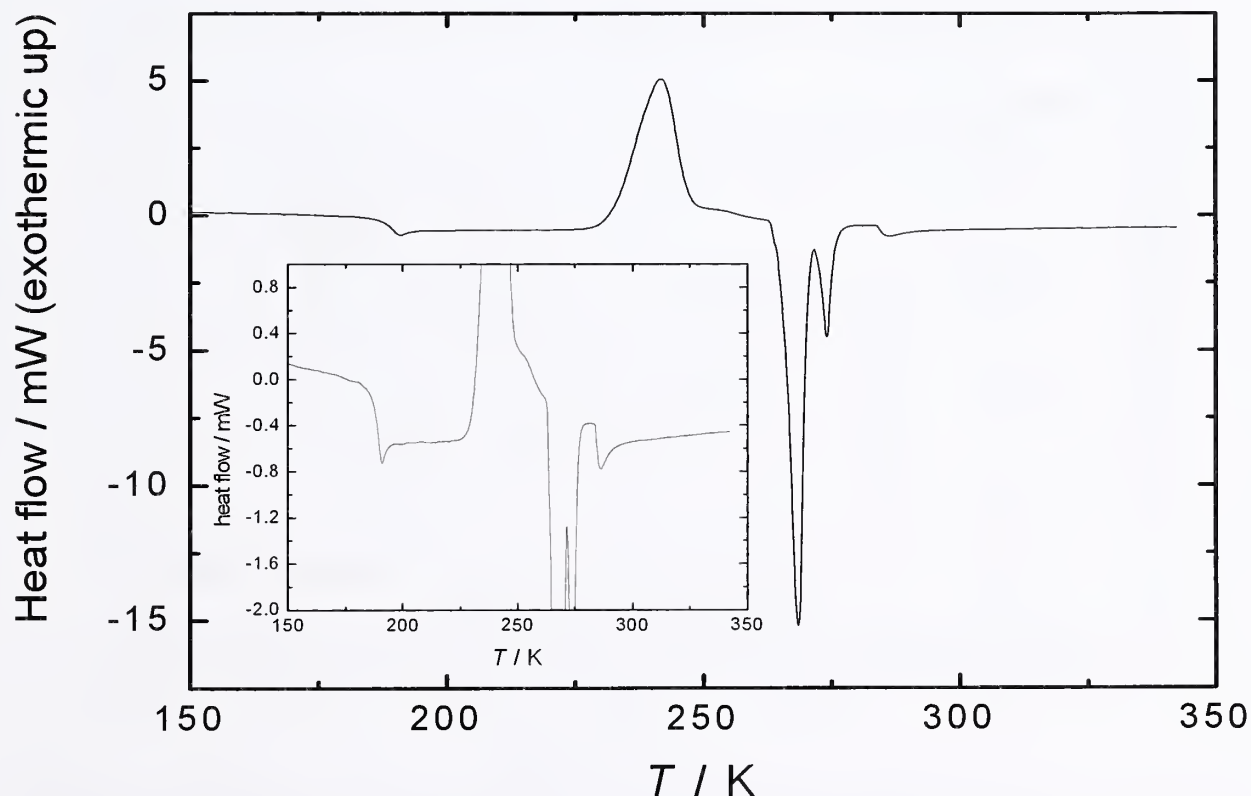


Figure 2. A typical thermal analysis curve for the ionic liquid with no tempering periods. Apparent are the glass transition near 190 K, an exothermic devitrification event beginning near 230 K, and multiple endothermic events above 260 K. (All stated temperatures are approximate.) The inset shows an expanded ordinate scale.

decomposition products; fast-scan TGA does not detect thermal decompositions at temperatures that do not yield products that are rapidly volatile at that temperature. There are also limitations with establishment of equilibrium for slow reactions, incorrectness of results for reactions that have induction periods, and errors from improper accounting for the temperature lag in the scanning experiment. Concern that most of the reported decomposition temperatures for room-temperature ionic liquids are misleading and/or incorrect for technical reasons has been expressed previously [10].

Our measurements of thermal behavior of the ionic liquid heated above 420 K showed signs of thermal decomposition. Figure 3 shows heat capacity values from a sequential series of temperature scans on the same sample following an initial conditioning period at 423 K. Above 400 K, the temperature dependence of the sample's heat capacity began to decrease, and at somewhat higher temperatures, the heat capacity began to decrease with increasing temperature. These effects are consistent with a slow exothermic reaction occurring in the sample. Each subsequent heat capacity curve showed a heat capacity smaller than that from the previous determination. Conducting a crude extrapolation of the sequence of heat capacity values at 298 K, including consideration of the pan conditioning scan, gave for the zero time value a heat capacity of approximately $1.4 \text{ J}\cdot\text{K}^{-1}\cdot\text{g}^{-1}$, which is close to the true value measured here (to be described below).

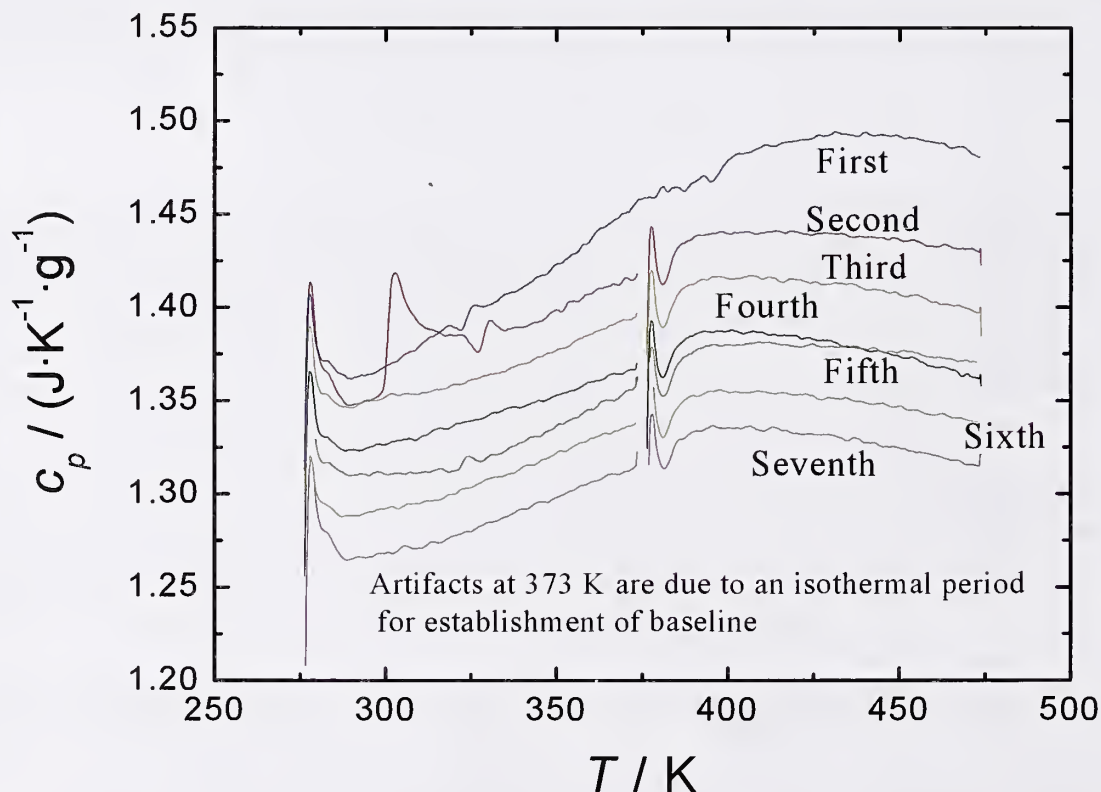


Figure 3. Sequential measurements of a single sample of the ionic liquid from 273 K to 473 K. The measurements show a decreasing heat capacity of the liquid above 430 K on the first scan and at lower temperatures on subsequent scans.

Figure 4 shows a collection of portions of thermal scans for the ionic liquid with different thermal histories. When the liquid is cooled to low temperature, a glass forms. Upon subsequent heating of the glass it converts to the supercooled liquid. The assigned glass transition temperature—where we have used the inflection point observed for the transition from glass to supercooled liquid—is $(189 \pm 0.5) \text{ K}$, where the uncertainty incorporates the fact that the inflection appears not so much as a point, but as a region of equal slope in the derivative curve. The heat capacity change accompanying the change of glass to supercooled liquid is approximately $0.38 \text{ J}\cdot\text{K}^{-1}\cdot\text{g}^{-1}$ at 189 K . The value for the heat capacity change from glass to liquid depends upon which temperature is selected for the calculation, due to the fact that the temperature dependences of the heat capacities of the glass and the liquid are different. We note that, for the purposes of quantitative comparison of numerical values from different studies, some points of relevance must be made. First, the values assigned to the glass transition temperature are operational, as it is well known that (1) a glass transition occurs over a temperature range, and (2) different characteristic temperatures (onset, midpoint, inflection, etc.) within this range may be reported as the glass transition temperature. The onset temperature for the transition depends on whether it is determined upon heating or cooling, and these will be quite different. The midpoint temperature or inflection temperature is often used, as these temperatures often correlate well with assigned glass transition temperatures obtained from other modalities, e.g., dynamic mechanical analysis.

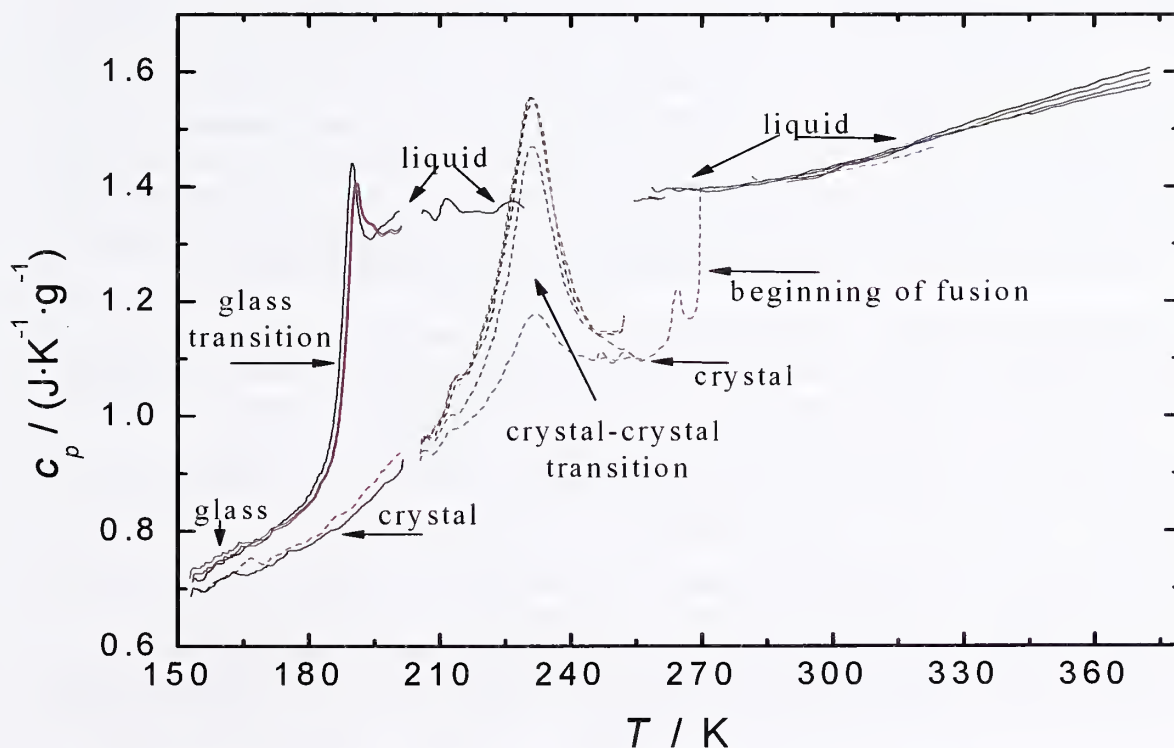


Figure 4. Heat capacity of various phases and forms of 1-hexyl-3-methylimidazolium bis(trifluoromethylsulfonyl)imide against temperature. Multiple determinations of the properties are shown in the figure. Also shown is an endothermic crystal transition, the magnitude of which depended on the tempering temperature reached prior to subsequent cooling to repeat the measurement.

The definition that we have used here, the inflection point for the transition, is quite often used. Quantitative comparison of properties of glasses and their transition processes is further complicated by the fact that the temperature range of the glass transition can depend upon the thermal history of a sample—moving to lower temperatures with slower cooling rates.

The heat capacity of the supercooled liquid was readily observed from 195 K to the temperature at which devitrification occurred, which is about 230 K. The ionic liquid could be supercooled to about 250 K without encountering a subsequent devitrification upon heating. Some heating scans for the supercooled liquid were begun near 250 K to obtain the heat capacity of the liquid in that temperature range.

If the temperature scan was halted after the devitrification event, before fusion, and the sample cooled again, then measurements of the heat capacity of a crystal phase could be obtained. This crystal phase had a lower heat capacity than had the glass. Heating of this crystal phase from 203 K to 253 K resulted in an exothermic event that we attributed to a crystal-crystal phase transition, as the enthalpy was fairly small, $\Delta_{\text{trs}}h = (4.9 \pm 0.50) \text{ J}\cdot\text{g}^{-1}$. The enthalpy of transition corresponded to an entropy change of $(9.4 \pm 1.0) \text{ J}\cdot\text{K}^{-1}\cdot\text{mol}^{-1}$. Reversibility was observed in that after passing through the event once by scanning from 203 K to 253 K, holding for 20 min at 253 K, followed by cooling to 203 K, and repeating the process gave reproducible thermal data. The uncertainty was calculated as the 95 % confidence interval of the means based on seven measurements spread over two samples of different masses. A smaller enthalpy change was obtained for this event if the sample's previous thermal history had extended from 203 K to 258 K, this being the curve with the obviously smaller enthalpy change at the transition temperature near 231 K. The heat capacity of the crystal with this thermal history appeared a bit smaller than the heat capacity of the crystal obtained from heating to 253 K and holding at that temperature for 20 min. Additionally, the thermal history affected how many peaks were observed around the fusion temperature and their relative magnitudes. We interpreted all of these observations to be consistent with the formation of at least two, and perhaps three, different crystal phases, but caution that one or more of them may not be a thermodynamically stable phase, but rather may be only a molecular arrangement that is kinetically trapped in a local energy minimum.

Heat capacity results for the glass, the liquid, and the low temperature and high temperature crystal phases are given in Tables 4 through 6. These values were calculated from the raw data after correction for the temperature error and the correction of the heat flux for both the temperature-scale error and the heat-flux error. Interpolation between the corrected temperatures, which are quite closely spaced, was performed to obtain values at the round temperatures given in the tables. These interpolations never exceeded 0.05 K.

Least-squares-estimated polynomials were used to represent the data in Tables 4 through 6. Rather than center the data prior to least-squares representations, we used functions that incorporated the centering, thereby giving realistic statistics for the fitted coefficients. The coefficients of the polynomials for the low-temperature and high-temperature crystal phases, the glass, and the liquid phase—both stable and supercooled—are given in Table 7.

Uncertainties were obtained from a combination of the reproducibility of the measurements and a contribution from the calibration information. For the liquid at 298 K, the 95 % confidence interval of the means was 0.35 % and the uncertainty arising from calibration of the heat flux was expected to be no more than 1 %. Propagation of these errors gave an uncertainty of 1.1 % at a 95 % confidence interval. At much lower temperatures (155 K), and as 373 K was

approached, precision between runs degraded to 1 % and 0.7%, respectively, while the calibration error increased to a maximum likelihood value of 2 % at 155 K but was unaffected at 373 K. Propagation led to uncertainties of the heat capacity values of 1.2 % at 373 K and 2.2 % at 155 K; values that are consistent with 95 % confidence intervals. These values can be used to construct a smooth set of uncertainty values for all of the heat capacity values calculated from the polynomials.

Determination of the enthalpy of fusion was complicated by the number of crystal phases and the concomitant need for extended tempering schedules. Tempering schedules with our DSC are limited to about 4 hours. The most obvious indication of unsuccessful tempering was the presence of a fusion event near 265 K. Table 8 gives fusion data for the 272.1 K fusion event, obtained with two different samples, one was 5 mg and the other was 13 mg. The observed fusion temperature for the apparently stable phase was (272.11 ± 0.29) K, where the uncertainty is a 95 % confidence interval. We expect that the enthalpy of fusion determination for this phase transition will not have a symmetrical probability distribution. Rather, because incomplete tempering will result in some small portion of the lower melting phase being present, incomplete tempering would shift the observed enthalpy to values slightly lower than the true value. The less stable phase has a fusion temperature of 265.8 K.

5. References

- [1] D. G. Archer, S. Rudtsch, Enthalpy of fusion of indium; a certified reference material for differential scanning calorimetry. *J. Chem. Eng. Data* 48: 1157-1163 (2003).
- [2] R. A. Ruehrwein, H. M. Huffman, Thermal data. XVII. The heat capacity, entropy and free energy of formation of cyclohexane. A new method of heat transfer in low temperature calorimetry. *J. Am. Chem. Soc.* 65: 1620-1625 (1943).
- [3] J. G. Aston, G. J. Szasz, H. L. Fink, The heat capacity and entropy, heats of transition, fusion and vaporization and the vapor pressures of cyclohexane. The vibrational frequencies of alicyclic ring systems. *J. Am. Chem. Soc.* 65: 1135-1139 (1943).
- [4] G. S. Parks, H. M. Huffman, S. B. Thomas, Thermal data on organic compounds. VI. The heat capacities, entropies and free energies of some saturated, non-benzenoid hydrocarbons, *J. Am. Chem. Soc.* 52: 1032-1041 (1930).
- [5] W. T. Ziegler, D. H. Andrews, The heat capacity of benzene-d₆. *J. Am. Chem. Soc.* 64: 2482-2485 (1942).
- [6] D. A. Ditmars, Calibration standards for differential scanning calorimetry I. Zinc: absolute calorimetric measurement of T_{fus} and $\Delta_{\text{fus}}H_{\text{m}}$. *J. Chem. Thermodynam.* 22: 639-651, (1990)
- [7] D. G. Archer, R. W. Carter, Thermodynamic properties of the NaCl + H₂O System. IV. Heat capacities of H₂O and NaCl(aq) in cold-stable and supercooled States. *J. Phys. Chem. B* 104: 8563-8584 (2000).
- [8] D. G. Archer, Thermodynamic properties of synthetic sapphire (α - Al₂O₃), standard reference material 720 and the effect of temperature-scale differences on thermodynamic properties. *J. Phys. Chem. Ref. Data* 22: 1441-1453 (1993).

[9] C. P. Fredlake, J. M. Crosthwaite, D. G. Hert, S. N. V. K. Aki, J. F. Brennecke, Thermophysical properties of imidazolium-base ionic liquids. *J. Chem. Eng. Data* 49: 954-964 (2004).

[10] M. Kosmulski, J. Gustafsson, J. B. Rosenhom, Thermal stability of low temperature ionic liquids revisited. *Thermochim. Acta* 412: 47-53 (2004).

Table 4. Heat capacity of crystal phases.

T/K	$c_p / (\text{J}\cdot\text{K}^{-1}\cdot\text{g}^{-1})$	$c_p / (\text{J}\cdot\text{K}^{-1}\cdot\text{g}^{-1})$
Low temperature		
153	0.6830	-
155	0.6987	0.6969
157	0.6984	0.7019
159	0.7133	0.7136
161	0.7193	0.7218
163	0.7282	0.7300
165	0.7245	0.7437
167	0.7271	0.7540
169	0.7330	0.7443
171	0.7487	0.7493
173	0.7505	0.7597
175	0.7622	0.7690
177	0.7667	0.7757
178	0.7680	0.7782
180	0.7755	0.7858
182	0.7855	0.7934
184	0.7965	0.8082
186	0.8030	0.8256
188	0.8120	0.8317
190	0.8270	0.8415
192	0.8422	0.8620
194	0.8539	0.8797
196	0.8708	0.8961
198	0.8851	0.9153
200	0.8957	0.9308
High temperature		
244	-	1.1000
246	1.0956	1.0976
248	1.1045	1.1014
250	1.0936	1.0973
252	1.1107	1.0999
254	1.1071	1.1019
256	1.0969	1.0996
258	1.1029	-

Table 5. Heat capacity of the glass.

T/K	$c_p / (\text{J}\cdot\text{K}^{-1}\cdot\text{g}^{-1})$	$c_p / (\text{J}\cdot\text{K}^{-1}\cdot\text{g}^{-1})$	$c_p / (\text{J}\cdot\text{K}^{-1}\cdot\text{g}^{-1})$
153	0.7281		
155	0.7362	0.7269	0.7138
157	0.7457	0.7374	0.7295
159	0.7571	0.7477	0.7438
161	0.7617	0.7561	0.7509
163	0.7712	0.7607	0.7586
165	0.7800	0.7738	0.7672
167	0.7805	0.7754	0.7796
169	0.7877	0.7804	0.7846
171	0.8020	0.7929	0.7920
173	0.8096	0.8049	0.8097
175	0.8159	0.8117	0.8221
177	0.8300	0.8238	0.8362
179	0.8424	0.8382	0.8497

Table 6. Heat capacity of the liquid.

T/K	$c_p / (\text{J}\cdot\text{K}^{-1}\cdot\text{g}^{-1})$				
196	1.3170	1.3258			
198	1.3187	1.3386			
200	1.3187	1.3546			
206	1.3561				
208	1.3481				
210	1.3545				
212	1.3773				
214	1.3619				
216	1.3554				
218	1.3570				
220	1.3544				
222	1.3543				
224	1.3651				
226	1.3739				
228	1.3707				
256		1.3766			
258	1.3821	1.3796			
260	1.3787	1.3779			1.3905
262	1.3832	1.3810			1.3967
264				1.3969	1.3934
266			1.3975	1.3963	1.3946
268			1.3998	1.3940	1.3955
270			1.3983	1.3955	1.3927
272			1.3969	1.3987	1.3920
274			1.3968	1.3990	1.3921
276			1.3994	1.3993	1.3951
278			1.4015	1.4016	1.3979
280			1.4033	1.4043	1.4022
282			1.4050	1.4067	1.4027
284			1.4083	1.4088	1.4048
286			1.4130	1.4125	1.4085
288			1.4159	1.4136	1.4109
290		1.4083	1.4174	1.4173	1.4141
292	1.4144	1.4110	1.4198	1.4198	1.4176
294	1.4157	1.4130	1.4251	1.4245	1.4219
296	1.4178	1.4147	1.4282	1.4285	1.4253

Table 6. Heat capacity of the liquid (cont.).

T/K	$c_p / (\text{J}\cdot\text{K}^{-1}\cdot\text{g}^{-1})$				
298	1.4211	1.4203	1.4316	1.4304	1.4283
300	1.4258	1.4277	1.4358	1.4357	1.4324
305	1.4423	1.4389	1.4456	1.4453	1.4417
310	1.4516	1.4481	1.4554	1.4549	1.4514
315	1.4671	1.4623	1.4618	1.4666	1.4633
320	1.4807	1.4769	1.4786	1.4784	1.4758
325	1.4941	1.4880	1.4917	1.4888	1.4882
330	1.5069	1.5015	1.5017	1.4984	1.4981
335	1.5197	1.5148	1.5134	1.5077	1.5093
340	1.5338	1.5275	1.5236	1.5180	1.5175
345	1.5443	1.5379	1.5319	1.5264	1.5286
350	1.5556	1.5496	1.5430	1.5368	1.5401
355	1.5690	1.5605	1.5532	1.5465	1.5506
360	1.5793	1.5695	1.5632	1.5550	1.5608
365	1.5909	1.5810	1.5712	1.5623	1.5706
370	1.6010	1.5924	1.5788	1.5707	1.5807

Contiguous measurement values are grouped within each column (i.e., a group of numerical values within a column that possesses no blank spaces is from one measurement series; blank spaces separate different measurement series). Breaks within any column represent noncontiguous measurement series. No chronological history is implied by the ordering of groups of values.

Table 7. Parameters for representations.

Parameter	Value	95 % conf. interval
Low temperature crystal - 153 K to 180 K		
$c_p / c_p^\circ = a + b(T / \text{K} - 167)$		
<i>a</i>	0.7364	0.0020
<i>b</i>	3.347E-3	2.7E-5
High temperature crystal - 244 K to 258 K		
$c_p / c_p^\circ = a$		
<i>a</i>	1.101	0.0025
Glass - 153 K to 179 K		
$c_p / c_p^\circ = a + b(T / \text{K} - 165) + c(T / \text{K} - 165)^2$		
<i>a</i>	0.7703	0.0041
<i>b</i>	4.373E-3	3.8E-5
<i>c</i>	4.644E-5	6.6E-7
Liquid - 196 K to 370 K		
$c_p / c_p^\circ = a + b(T / \text{K} - 283) + c(T / \text{K} - 283)^2 + d(T / \text{K} - 283)^3$		
<i>a</i>	1.411	0.0043
<i>b</i>	1.2588E-3	7.2E-6
<i>c</i>	7.9137 E-6	3.8E-10
<i>d</i>	2.86618E-8	2.6E-13

$$c_p^\circ = 1 \text{ J}\cdot\text{g}^{-1}$$

Table 8. Temperature of fusion and enthalpy of fusion of apparent stable phase.

Sample	$\Delta_{\text{fus}}H / (\text{J}\cdot\text{g}^{-1})$	$T_{\text{fus}} / \text{K}$
13 mg	61.64	271.46
13 mg	61.61	272.09
5 mg	61.73	272.10
5 mg	62.60	272.51
5 mg	62.95	272.20
5 mg	62.63	272.32
Average and 95 % conf. interval	62.20 ± 0.49	272.11 ± 0.29

